HHS Public Access

Author manuscript

Acta Biomater. Author manuscript; available in PMC 2023 September 15.

Published in final edited form as:

Acta Biomater. 2022 September 15; 150: 295–309. doi:10.1016/j.actbio.2022.07.036.

Linking the region-specific tissue microstructure to the biaxial mechanical properties of the porcine left anterior descending artery

Sergio A. Pineda-Castillo[a,b], **Santiago Aparicio-Ruiz**[a], **Madison M. Burns**[a], **Devin W. Laurence**[a], **Elizabeth Bradshaw**[a], **Tingting Gu**[c], **Gerhard A. Holzapfel**[d,e], **Chung-Hao Lee**[a,*]

[a]Biomechanics and Biomaterials Design Lab, School of Aerospace and Mechanical Engineering, The University of Oklahoma, USA

[b]Stephenson School of Biomedical Engineering, The University of Oklahoma, USA

[c]Samuel Roberts Noble Microscopy Laboratory, The University of Oklahoma, USA

[d]Institute of Biomechanics, Graz University of Technology, Austria

[e]Department of Structural Engineering, Norwegian University of Science and Technology, Norway

Abstract

Coronary atherosclerosis is the main cause of death worldwide. Advancing the understanding of coronary microstructure-based mechanics is fundamental for the development of therapeutic tools and surgical procedures. Although the passive biaxial properties of the coronary arteries have been extensively explored, their *regional* differences and the relationship between tissue microstructure and mechanics have not been fully characterized. In this study, we characterized the passive biaxial mechanical properties and microstructural properties of the proximal, medial, and distal regions of the porcine left anterior descending artery (LADA). We also attempted to relate the biaxial stress-stretch response of the LADA and its respective birefringent responses to the polarized light for obtaining information about the load-dependent microstructural variations. We found that the LADA extensibility is reduced in the proximal-to-distal direction and that the medial region exhibits more heterogeneous mechanical behavior than the other two regions. We have also observed highly dynamic microstructural behavior where fiber families realign themselves depending on loading. In addition, we found that the microstructure of the distal region exhibited highly aligned fibers along the longitudinal axis of the artery. To verify this microstructural feature, we imaged the LADA specimens with multi-photon microscopy and observed that the adventitia microstructure transitioned from a random fiber network in the proximal region to highly aligned fibers in the distal region. Our findings may offer new perspectives for understanding coronary mechanics and aid in the development of tissue-engineered vascular grafts, which are currently limited due to their mismatch with native tissue in terms of mechanical properties and microstructural features.

*Corresponding author. 865 Asp Ave., Felgar Hall 219C, Norman, OK 73019, USA. ch.lee@ou.edu (Chung-Hao Lee).

Declaration of Competing Interest. The authors declare that they have no known competing financial interests or personal relationships that could have appeared to influence (bias) the work reported in this manuscript.

Keywords

coronary artery biomechanics; polarized spatial frequency domain imaging; planar biaxial testing; multi-photon microscopy; collagen and elastin microstructure

1. Introduction

Coronary heart disease (CHD) is the main cause of death in the United States with an annual prevalence of 7.2% (CI: 6.5-7.9%) [1]. CHD amounts for 42% of all cardiovascular-related deaths with approximately 360 000 annual cases [1]. CHD is caused by atherosclerosis, an inflammatory disease that leads to occlusion of the coronary arteries and eventual myocardial infarction. CHD can be treated with strategies ranging from lifestyle management to the use of therapeutic drugs, percutaneous angioplasty, and/or revascularization strategies [2, 3]. Therapeutic agents may include beta-blockers, statins, anti-platelet agents, among others. On the other hand, percutaneous angioplasty, known as coronary stent implantation, involves the use of drug-eluting metal stents to mechanically restore the vessel diameter. Angioplasty is typically limited to treating a *single* coronary artery disease, a non-tortuous coronary anatomy, and mild to moderate occlusions. In the case of multiple, severe occlusions and complex arterial anatomies, coronary artery bypass grafting (CABG) is the preferred method to restore coronary blood flow [3]; see [2] for a complete review of current CHD therapies.

CABG was introduced in 1967 by Dr. René Favaloro as an alternative to revascularization of atherosclerotic coronary arteries [4]. Since then, CABG has been the most effective treatment for advanced and multiple atherosclerotic coronary arteries [3]. In this procedure, an arterial or venous autograft is used to bypass the occlusion at the coronary artery. Despite the current wide variety of autograft sources [3, 5-8], clinicians face challenges in the selection and availability of grafts for the bypass procedure. Other difficulties encountered are geometric mismatch [9-11], de-endothelization [12], loss of patency [13], and unavailability of autologous grafts due to previous CABG [14]. Therefore, there is a critical need for technological developments to provide non-autologous graft sources such as tissue-engineered vascular grafts (TEVGs).

Vascular tissue engineering (VTE) aims to fabricate functional vascular conduits for bypass. Current advances in VTE have allowed the implantation of non-small-diameter (> 6 mm) TEVGs [15], but small-diameter conduits still have limitations due to compliance mismatch, the lack of functional elastin and thrombogenesis [16-18]. In particular, a mismatch between the mechanical properties of the TEVG and the target vessel is a critical issue in VTE. However, the design and characterization of TEVGs are often limited to the burst pressure and suture strength [19-21], and little attention is paid to the native biaxial mechanical properties of the target artery, its collagen/elastin microstructure, and more importantly, the relationship of these features to the *in vivo*-equivalent biaxial stresses exerted by blood flow. In addition, the TEVG design is further limited by a lack of knowledge of the region-specific mechanical requirements of the coronary arteries. Finally, CABG requires the selection of anastomotic sites for connection of the grafts to the native vessel.

Such selection consideration is critical for long-term graft patency [3, 22, 23], but the microstructural and mechanical properties of the potential sites (i.e., arterial regions) have not been systematically studied. The investigation of these region-specific properties of the coronary vasculature could also support the development of patient-specific models for CHD diagnostics and the simulation of TEVG implantation [24-26].

Therefore, the TEVG design should also consider the region-specific properties of the target vessel to more accurately mimic the mechanics and microstructure of the anastomotic site and reduce the chances for graft failure. In this study, we characterize the region-specific microstructural and mechanical properties of the porcine left anterior descending artery (LADA). We present the unique region-specific properties of the LADA, including the load-dependent microstructural properties of the vessel. Collectively, these results will provide new insights into microstructure-based arterial biomechanics that may potentially aid in the development of TEVGs as well as the selection of anastomotic sites for CABG.

2. Methods

2.1. Tissue Acquisition and Preparation

Porcine hearts (n = 14, 80-140 kg, 1-1.5 years of age) were obtained from a local, USDA-approved slaughterhouse (Chickasha Meat Company, Chickasha, OK, USA). Upon arrival at our lab, the hearts were dissected and the LADA specimens harvested by excising the surrounding myocardium and connective tissue (Fig. 1(a)). Then the isolated artery tissue (Fig. 1(b)) was placed with the pericardium facing the dissecting board, followed by longitudinal incisions to trim down the surrounding myocardium and connective tissue to expose the complete artery (Fig. 1(c)). Thereafter, the exposed artery was cut immediately after the bifurcation of the main left coronary artery. Then, the exposed LADA was marked with a surgical pen to delineate its proximal, medial and distal third. Finally, the artery was delicately separated from the surrounding tissue (Fig. 1(d)) and cut into the marked thirds (not shown). The resulting LADA tissue regions were then classified as *proximal, medial* and *distal,* relative to their proximity to the aorta (Fig. 1(c)). If specimens were not tested after dissection, they were temporarily stored in a freezer (−20 °C) until biaxial mechanical testing and collagen microstructural quantification (within 48 h of dissection) [27].

2.2. Tissue Preparation for Characterizations

Tissues were thawed in phosphate-buffered saline (PBS) at room temperature (~ 23 °C) and the stress-free outer diameter of the vessel was measured with a caliper (Westward Tools, resolution: 0.01 mm). The cylindrical specimen was cut open with dissecting scissors and a testing region was selected based on the lack of outlets to avoid tissue tearing during testing. This region varied in size per specimen, but special care was taken to maintain a distance of > 1 mm between the edge of two adjacent tissue specimens tested.

The test region was then cut and tissue thickness was measured at three different locations using a non-contact laser displacement sensor (Keyence IL-030, Itaska, IL, USA) to calculate the mean tissue thickness. The specimen was next labeled with a surgical pen to ensure the proper alignment of the specimen with the test directions of a commercial

biaxial testing system (BioTester, CellScale, Canada). Using BioRake tines, specimens were mounted on the system, where the circumferential direction was aligned with the x-axis of the BioTester, resulting in an effective test region of 6.5 × 6.5 mm for the proximal and medial regions and 4.5 × 4.5 mm for the distal region (Fig. 2(a)). Once mounted, four glass beads (diameter of 300-500 μm) were glued to the top surface of the specimen, which served as fiducial markers for the quantification of tissue in-plane strains (Fig. 2(a)).

2.3. Biaxial Mechanical Testing

LADA specimens were submerged in a PBS bath at 32 °C during all biaxial testing procedures. This temperature was chosen to match *in vivo* conditions while preventing fog from accumulating on the lens of the rotational polarizer. In the biaxial mechanical testing, specimens were first subjected to a preconditioning protocol. This protocol consisted of fifteen force-controlled loading-unloading cycles with a displacement rate of ~ 100 μm/s, where a targeted first Piola-Kirchhoff (1st PK) stress P_{max} of 120 kPa was used to restore the tissue to its *in vivo* functional configuration and achieve repeatable stress-stretch curves [28-30]. After preconditioning, biaxial testing was performed using a series of displacement-controlled protocols to target various 1st PK stress ratios (P_{CC}:P_{LL} = 1:1, 1:0.75, 1:0.5, 1:0.25, 0.5:1, 0.75:1), which were used to characterize a wide range of possible tissue biaxial deformations. Each loading/unloading protocol (Fig. 2(b)) was repeated three times, measuring the force from the load cells and capturing the deformation of the fiducial markers with a CCD camera at a frequency of 15 Hz. Next, tissue stress-stretch calculations were performed using the 3rd loading/unloading cycle of each biaxial loading ratio.

2.4. Calculations of Tissue Strain and Stress

The in-plane tissue strains were calculated following the procedures described in our previous biaxial testing studies [31, 32]. Using the images captured by the CCD camera, the time-dependent positions of the fiducial markers were tracked using the digital image correlation (DIC) module of the BioTester's LabJoy Software (CellScale, Canada), i.e.

$$\mathbf{x}_I(t) = \mathbf{X}_I + \mathbf{d}_I(t), \quad I = 1, \ldots, 4, \tag{1}$$

where $\mathbf{X}_I$ and $\mathbf{x}_I(t)$ are the fiducial marker positions at the undeformed Ω_0 and deformed Ω_t configurations, respectively, and $\mathbf{d}_I(t)$ is the vector of displacements of marker I along the x- and y-axes, with components $u_I(t)$ and $v_I(t)$. In this work we have chosen Ω_0 as the post-preconditioning (PPC) configuration.

Then, the deformation gradient $\mathbf{F}$ was determined using a four-node bi-linear finite element in MATLAB (Mathworks, CA, USA) [31], which reads in matrix notation

$$[\mathbf{F}] = [\mathbf{F}(\mathbf{X}, t)] = [\mathbf{I}] + \begin{bmatrix} \sum_{I=1}^{4} B_{xI} u_I(t) & \sum_{I=1}^{4} B_{yI} u_I(t) \\ \sum_{I=1}^{4} B_{xI} v_I(t) & \sum_{I=1}^{4} B_{yI} v_I(t) \end{bmatrix}. \tag{2}$$

Herein, B_{xI} and B_{yI} are the shape function derivatives with respect to the x- and y-coordinates for the node (marker) I, respectively. Then the right Cauchy-Green tensor **C** and the Green-Lagrange strain tensor **E** were calculated as

$$\mathbf{C} = \mathbf{F}^{\mathrm{T}}\mathbf{F} \quad \text{and} \quad \mathbf{E} = \frac{1}{2}(\mathbf{C} - \mathbf{I}), \tag{3}$$

where **I** is the second-order identity tensor. Note that the tine-based tissue attachment induce negligible shear deformation in our biaxial testing procedures, given the inherent rigidity of the BioRakes and the specimens' circumferential fibers of the tunica media oriented along the x-axis of the BioTester [33]. Next, the principal values of **C** were used to calculate the circumferential (λ_{C}) and longitudinal (λ_{L}) stretches. From this, the anisotropy index was determined as $AI = \lambda_{\mathrm{L}} / \lambda_{\mathrm{C}}$. Finally, the 1st PK stress was calculated from the forces F_{C} and F_{L}, the effective edge length L, and the average tissue thickness t according to

$$[\mathbf{P}] = diag[P_{\mathrm{CC}}, P_{\mathrm{RR}}] = \frac{1}{tL}\begin{bmatrix} F_{\mathrm{C}} & 0 \\ 0 & F_{\mathrm{L}}. \end{bmatrix} \tag{4}$$

The stress-stretch curves were further used to determine parameters based on tissue mechanics (Fig. 2(c)): the low- and high-tension elastic moduli E^{LT} and E^{HT}, and the tissue extensibility λ^*. E^{HT} was obtained as the slope of the linear curve fitted to the last 15-20% stress-stretch data points, while λ^* is the intersection with the x-axis of the linear regression. The same procedure was repeated to determine E^{LT} via the linear fit to the first 20-25% data points.

2.5. Characterization of the Fiber Architecture – Polarized Imaging in the Spatial Frequency Domain

Microstructural characterization of the LADA specimens was performed using an in-house polarized spatial frequency domain imaging (pSFDI) system (Fig. 2(a)) integrated with the BioTester, based on our previously developed protocol [32, 34, 35], which allows an evaluation of the tissue's *load-dependent* collagen fiber architecture. Briefly, the incident light was emitted using a LED projector with spatial frequency patterns (Texas Instruments, Dallas, TX) with a cyan light (wavelength of 490 nm). Each specimen was imaged using a 5-megapixel CCD camera (Basler, Germany) coupled to a rotating linear polarizer (Thorlabs Inc., Newton, NJ) to record the back-scattered light intensity response with respect to polarization angle (0-180° at 5° increments) [36, 37]. To further examine the load-dependent changes in collagen fiber architecture, the LADA specimens were imaged at the peak load of each of the biaxial testing protocols (see Section 2.3). In addition, the specimens were also imaged at six loading points of the equibiaxial tension protocol (P_{CC}:P_{LL} = 1:1) and the P_{CC}:P_{LL} = 1:0.5 protocol, where these imaged points were defined as:

- **i.** Loading Point 0: Post-preconditioning configuration (PPC) configuration Ω_0.
- **ii.** Loading Points 1-3: Three evenly spaced points between Loading Points 0 and 4.
- **iii.** Loading Point 4: 30% of peak stress $P_{\max}$.

iv. Loading Point 5: Fully loaded configuration (i.e., P_{max}).

In this pSFDI-based microstructural quantification of collagen, the pixel-by-pixel fiber orientation angle (θ_{fiber}) and the degree of optical anisotropy (DOA) were determined [34]. The DOA describes the alignment of fibers: a larger DOA value indicates a greater alignment of the collagen architecture; see Appendix A for more details on determining the DOA.

2.6. Constitutive Modeling

The biaxial behavior of the regional LADA tissue was modeled using a simplified two-dimensional strain-based Fung-type model proposed by Keyes and van de Geest *et al.* [38], i.e.

$$W = \frac{c}{2}\left[\exp\left(a_1 E_{XX}^2 + a_2 E_{XX}^2 + a_3 E_{XX} E_{YY}\right) - 1\right], \tag{5}$$

where W is the strain-energy function, c, a_1, a_2, and a_3 are the model parameters, and E_{XX} and E_{YY} are the Green-Lagrange strains along the x- (circumferential) and y- (longitudinal) directions, respectively. The first PK stress can then be computed from Eq. (5) by $\mathbf{P} = \mathbf{F}\partial W / \partial \mathbf{E}$ (note that (5) can be replaced by any other constitutive law that captures more complexity).

The model parameters were determined by non-linear least squares regression to the biaxial mechanical data. The error function was minimized with an in-house differential evolution optimization algorithm [39], i.e.

$$e_j^2 = \frac{1}{n_{data}}\left[\sum_{i=1}^{n_{data}} \left(P_{XX,i}^{data} - P_{XX,i}^{model}\right)^2 + \left(P_{YY,i}^{data} - P_{YY,i}^{model}\right)\right], \qquad j = 1, \ldots, n_{pop}, \tag{6}$$

where e_j denotes the error for the j-th parameter set of the total n_{pop} sets of parameters, n_{data} is the number of experimental data points, and the superscripts (i.e. ‘data’ or ‘model’) denote either the experimental data or the model prediction. Finally, the parameter bounds were set to ensure a positive definite elasticity tensor, i.e., the convexity condition of our constitutive modeling.

2.7. Optical Clearing and Multi-Photon Microscopy

The specimens ($n = 3$) were dehydrated immediately after biaxial testing and pSFDI imaging using a graded ethanol series. Tissues were submerged in ethanol/PBS solutions at 50%, 75%, 100%, and 100% (v/v) for 30 min per grade level. Optical clearing was then performed using a 1:2 benzyl alcohol/benzyl benzoate (BABB) graded solution: 50%, 50%, 100%, 100% – BABB/ethanol (v/v) for 30 min per solution [40]. Optically transparent tissues were then mounted on a glass slide with double-sided tape to create a reservoir (~ 300 μm in height) in which to contain the tissue and 100% BABB solution during subsequent multi-photon imaging. Fiber architecture information of the LADA specimens were obtained through multi-photon microscopy. Tissue autofluorescence and second harmonic generation (SHG) signals were captured in a confocal/multiphoton dual system (Leica SP8 MP,

Germany) with an 80 MHz pulsed Ti: Sapphire laser (Chameleon, Coherent Inc., USA), tunable between 680 nm to 1080 nm. An excitation wavelength of $\lambda_{ex} = 830$ nm with 10 fs pulse width was used with an emission window set at $\lambda_{em} = 500\text{-}550$ nm for the autofluorescence (AF) signal. For SHG, we used $\lambda_{ex} = 830$ nm and $\lambda_{em} = 410\text{-}420$ nm. Image *z*-stacks of AF signal were collected (Fig. 2(d)) through a 20x multi-immersion objective with 0.75 NA, and then processed in ImageJ (National Institutes of Health) via the OrientationJ plugin to analyze the distribution of orientations of each image [41, 42], and the heat maps depicting fiber orientation distribution across tissue depth were generated using a custom MATLAB program. The SHG and AF signals were used to quantify the SGH/AF ratio to obtain a quantification of the collagen content in the specimens.

2.8. Sample Size Calculation and Statistical Analysis

The sample size was determined by performing a power analysis based on the preliminary tests of LADA specimens ($n = 3$). Using the preliminary differences in peak stretch at the circumferential direction λ_C, we calculated the sample size with one-way ANOVA using power analysis in GPower software (v3.1.9.7, Düsseldorf, Germany) [43]. The preliminary differences provided an effect size of ~ 0.65. With $\alpha = 0.05$ and a statistical power of $1 - \beta = 0.95$, we determined a sample size of $n = 14$ per tissue region for our experiments. All measurements are shown as mean ± standard error of the mean (SEM). Data normality was tested using the Shapiro-Wilk test and Q-Q plots. Then, depending on normality, the LADA regions were compared using one-way ANOVA or the Kruskal-Wallis test. For two factorial designs (LADA region vs. tissue direction), a two-way ANOVA or an aligned rank transform was used depending on normality [44]. Statistical significance was assumed when $p < 0.05$. All statistical assessments were performed in R (v4.1.1, R Foundation).

3. Results

3.1. Arterial Wall Geometry

The measured thickness was 388 ± 27 μm, 439 ± 42μm and 289 ± 10 μm for the proximal, medial, and distal regions, respectively (Fig. 3(a)), where the distal region is significantly thinner than the other two regions ($p = 0.004$). While the differences in thickness between the proximal and medial regions were not significant, the specimens of the medial region exhibited larger numeric values with greater variance. There was also a significant reduction in vessel diameter from proximal to medial and then to distal regions ($p < 0.001$): 3.05 ± 0.06 mm, 2.58 ± 0.07 mm, and 2.27 ± 0.11 mm.

3.2. Biaxial Mechanical Testing Results

Preconditioning of the LADA specimens resulted in a PPC stretch: $\lambda_{PPC} = 1.14 \pm 0.01$ (proximal), 1.12 ± 0.01 (medial), and 1.21 ± 0.01 (distal) (Fig. 3(b)), where the distal region shows a significantly larger PPC stretch than the other two regions ($p < 0.0001$). The PPC stretch in the longitudinal direction was found to be greater than in the circumferential direction, although the differences were not significant ($p = 0.06$).

Material anisotropy was consistently observed across all LADA regions. In general, the medial region showed a larger anisotropy ratio (λ_L / λ_C) than the proximal and distal regions.

Interestingly, some specimens showed the greater anisotropy along the *circumferential* direction (i.e. $\lambda_L / \lambda_C < 1$). In addition, the tissue anisotropy was dependent on the loading ratio (P_{CC}:P_{LL}), i.e. an increase in λ_L / λ_C when the loading ratios transitioned from circumferentially to longitudinally dominant loading protocols (Fig. 3(c)).

The LADA stress-stretch curves from biaxial mechanical tests exhibited a nonlinear anisotropic response with narrow hysteresis loops (Fig. 2(c)) as described previously for other coronary artery tissues (including human and other coronary arteries) [28, 45]. The biaxial stress-stretch curves were further used to quantify the mechanical parameters of each specimen (Fig. 2(d)). Under low-stresses (< 20-30 kPa), the specimens showed a compliant behavior (characterized by the low-tension moduli E^{LT}) until they reached a transition point where the stress increased exponentially and a mechanically stiffer response was observed (Fig. 4). In general, tissue stretch at peak loading decreased from proximal to distal: $\lambda_C = 1.30 \pm 0.02$ (proximal), 1.25 ± 0.02 (medial), and 1.27 ± 0.03 (distal) (Fig. 4), where the lowest values of LADA tissue extensibility were observed in the distal region. In contrast, longitudinal stretch did not vary as much between regions ($\lambda_L = 1.31 \pm 0.01$; $p = 0.36$), although the distal region was found to be the least extensible (Fig. 4). Furthermore, it was found that tissue extensibility does not vary significantly across different LADA regions and tissue directions ($\lambda^* = 1.19 \pm 0.01$; Fig. 5(a), Table S1). Finally, it was found that the moduli for the equibiaxial tension protocol in the LADA regions are similar under low-tension: $E^{LT} = 0.20 \pm 0.01$ MPa with non-significant variations across regions and tissue directions, but different under high-tension: E_C^{HT} significantly higher than E_L^{HT}(1.71 ± 0.11 MPa vs. 1.16 ± 0.10 MPa; $p < 0.001$). In particular, E_C^{HT} was significantly higher than E_L^{HT} for the proximal and medial regions, while no significant differences were observed in the distal region. This indicated a more isotropic behavior for the distal region of the LADA.

Let us now consider the mechanical behavior of the LADA under the *in vivo* functional condition, which is most representatively captured by the P_{CC}-P_{LL} = 1:0.5 loading protocol [46, 47]. E^{LT} for the LADA specimens was fairly homogeneous across different regions and tissue directions (Table S1, Fig. 5(b)). In contrast, E_C^{HT} was significantly higher than E_L^{HT} (1.99 ± 0.11 MPa vs. 0.88 ± 0.06 MPa; $p < 0.001$, Table S1, Fig. 5(b)). For tissue stretch λ under P_{CC}:P_{LL} = 1:0.5, the medial region was the least compliant and the proximal and distal regions showed similar behavior ($p = 0.31$, Table S1). On the other hand, λ_C was significantly larger than λ_L (1.31 ± 0.02 vs. 1.25 ± 0.01, $p = 0.007$). Finally, it was also found that the tissue extensibility λ_C^* is significantly greater than λ_L^* (1.21 ± 0.01 vs. 1.14 ± 0.01, $p < 0.001$).

The mechanical responses of the LADA tissue under other non-equibiaxial protocols were found to depend on the dominant loading axis (Fig. 4). Especially when the specimens were exposed to the dominant load in the circumferential direction (P_{CC}:P_{LL} = 1:0.75, 1:0.5, 1:0.25), tissue stretch increased in the circumferential direction and decreased in the longitudinal direction compared to the equibiaxial loading (Table S1). Likewise, tissue stretch increased in the longitudinal direction and decreased in the circumferential direction under radially dominant loading (P_{CC}:P_{LL} = 0.75:1, 0.5:1, 0.25:1). In general, the proximal

region exhibited greater tissue stretches than the other two LADA regions, while the medial region was the least extensible at all the biaxial loading ratios.

To further explore the mechanical response of the LADA regions, we modeled the biaxial mechanical data using hyperelasticity-based constitutive modeling. We obtained the model parameters (c, a_1, a_2, and a_3) for each specimen (Table S2) and the ones by fitting to the averaged experimental data as shown in Fig. 4. From these estimated parameters, we observed similar behaviors as described previously: the proximal region was the most compliant region in the circumferential direction, while the distal region was the stiffest in the longitudinal direction (see also Table S2 and Figure S6). Further, we quantified the stored strain energy associated with an equibiaxial stress state of 120 kPa and made comparisons between the three regions. We observed that stored energy decreased in the proximal-to-distal direction (Proximal vs. Medial: $p = 0.07$; Medial vs. Distal: $p < 0.05$, Table S2), indicating a decrease in the elastic behavior of the artery. These behaviors can be explained by a progressive change in the microstructure of the LADA regions, such as the greater fiber alignement, more homogeneous crimping or a lower degree of fiber crimping. Overall, the constitutive modeling helped confirm the findings of the mechanical behavior of the LADA regions presented in Section 3.2.

3.3. Arterial Microstructure

3.3.1. pSFDI Microstructural Characterizations: Load-Dependent Changes in the Fiber Alignment—The load-dependent microstructural architectures of the LADA regions were characterized using pSFDI. In general, we observed an increase in DOA with increased tissue stretch across all loading protocols. Figure 6 shows a representative specimen of each region at different loading points with equibiaxial loading. DOA increased from the first loading point (*Loading Point 1*) to the peak loading point (*Loading Point 5*) ($p < 0.001$) in all three regions, indicating fiber uncrimping and recruitment. The DOA at Loading Point 5 also also increased from proximal to distal (Fig. A1(a)): 7.4 ± 3.1% (proximal), 11.6 ± 4.4% (medial), and 24.5 ± 2.4% (distal) ($p = 0.002$ for distal vs. proximal).

For the P_{CC}:P_{LL} = 1:0.5 loading ratio, the DOA did not change across different loading points for the distal region, indicating that this loading ratio does not cause significant changes in the collagen architecture (Fig. A1(b)). For the medial region, the DOA increased by only 4.6 ± 3.5%, but the changes proved not to be statistically significant. However, we observed significant changes in the DOA for the proximal region with a 21.2 ± 2.7% increase ($p < 0.001$). On the other hand, under P_{CC}:P_{LL} = 0.5:1 there was an average reduction in DOA, although not significant, for the distal and medial regions (Fig. A1(c)), while the DOA for the proximal region increased significantly.

Considering other biaxial loading ratios (P_{CC}:P_{LL} = 0.75:1 and P_{CC}:P_{LL} = 1:0.75), there was a similar trend showing non-significant changes in DOA for the medial and distal regions along with a significant increase in DOA for the proximal region. Under P_{CC}:P_{LL} = 1:0.25 there were no significant changes in DOA for the distal region, while DOA increased in the medial and proximal regions: 10.4 ± 3.6% and 24.7 ± 3.9%, respectively ($p < 0.001$). Eventually, although we observed no significant changes in the DOA for the LADA regions

under longitudinally dominant loading (i.e., P_{CC}:P_{LL} = 0.25:1), there was a subtle reduction in the DOA of around 2-5%; see Fig. S1 for the changes in DOA under non-equibiaxial loading.

3.3.2. pSFDI Microstructural Characterizations: Load-Dependent Changes in the Fiber Orientation—From the histograms of the pSFDI-quantified fiber orientation θ_{fiber} (see Fig. S2) we typically observed two clear peaks in the distribution of the fibers: (i) a fiber family ranging from (−90°, −45°), with a peak of about −60°, and (ii) the second fiber family, oriented in the range of (30°, 60°) and reaching a peak at 45°. The location and dispersion of these two fiber families showed changes over different loading points and under different P_{CC}:P_{LL} loading ratios. These changes were further quantified using a π-periodic bi-modal von Mises distribution (see more details in Appendix B and our previous paper on pSFDI theory/analysis [34] and some representative results in Fig. S2), where the distribution parameters were obtained by nonlinear least-squares regression: μ_j's represent the angular location of the two fiber families, κ_j's denote the dispersion of their respective distributions, and w is the weight of the orientation density for the first fiber family.

Figure 7(a) shows the changes in θ_{fiber} between the two fiber families with an equibiaxial loading (P_{CC}:P_{LL} = 1:1) and the two extreme loading ratios (P_{CC}:P_{LL} = 1:0.25 and 0.25:1). Here the normalized fiber distance, denoted $|\mu_1 - \mu_2| / 90^{\circ}$, yielded a metric in the range of 0.0 (i.e. no difference in fiber families and hence a highly aligned microstructure) to 1.0 (i.e. two distinct, orthogonal fiber families). The normalized distance of fiber family at PPC (approximate *in vivo* configuration) revealed a more random organization of fiber families in the proximal and medial regions (Fig. 7(a)), while equibiaxial loading resulted in an increase in normalized fiber distance for the proximal and medial regions, suggesting that the two fiber families became more separated. Interestingly, the P_{CC}:P_{LL} = 1:0.25 loading protocol further increased the fiber family distance, indicating that fiber rearrangement occurred upon loading along the circumferential direction. Finally, we observed a reduction in the normalized fiber distance under P_{CC}:P_{LL} = 0.25:1 compared to the PPC configuration.

Uniquely, we observed that some distal specimens exhibited a behavior similar to the proximal and medial regions, while some other specimens exhibited the two fiber families with relatively small angular differences. Interestingly, we also observed for some distal specimens that the normalized fiber distance at PPC was close to 0 (Fig. 7(a)), indicating the presence of closely arranged fiber families and a higher degree of fiber alignment. Equibiaxial loading resulted in a slight decrease in the normalized fiber distance, while P_{CC}:P_{LL} = 1:0.25 loading increased the median distance. In contrast, the P_{CC}:P_{LL} = 0.25:1 loading further reduced the normalized distance.

The bi-modal von Mises distribution fit also provided information on the weight values (i.e. w for the first fiber family and $1 - w$ for the other) indicating the relative orientation densities between the two fiber families (Fig. 7(b)). Here, a change in w indicates an increase/decrease in the birefringence properties of the fibers, which can be represented by an increase/reduction in the alignment of each fiber family, as well as fiber uncrimping. We

observed the unique changes in weight values across the LADA regions: (i) the proximal region showed an increase in w under equibiaxial loading, which can be explained by the uncrimping of collagen fibers and reorganization of both fiber families; then, under the extreme loading ratios, a decrease in w was observed, indicating increased recruitment to one of the fiber families; (ii) the medial and distal regions show slight changes in w that were less pronounced than in the proximal region.

3.3.3. Microstructural Characterization – Multi-Photon Microscopy—The microstructure observed by multi-photon microscopy for the individual layers of the LADA was consistent with the traditional structure for the vessel wall: (i) the tunica intima was found as a collection of longitudinally oriented elastin bundles, and (ii) the tunica media had circumferentially aligned elastin fibers and lamellae (Fig. S3). Overall, we did not observe any evidence of freezing-induced damage or microcracks in the layered structure of the specimens (see exemplary multi-photon micrographs in Fig. S3). We also observed *region-specific* microstructures for the tunica adventitia. The adventitia is generally described as a random distribution of collagen and elastin fibers observed in the proximal region (Fig. 8, *top panel*). However, we further observed that the fiber distribution became more and more longitudinally aligned with increasing descent into the distal region (Fig 8, *top panel*). This interesting observation was confirmed with several LADA specimens as shown in Fig. S3 and across the entire transmural adventitia. Figure 8 (*bottom panel*) shows the fiber distribution over the entire tissue depth of three different specimens. All specimens exhibited a ‘core’ in the central area of the heat map, approximately at (−45°, 45°), representing the circumferential direction of the tissue. This core of the heat map represented the aligned fibers of the tunica media and its helical structure across the arterial wall. Below these ‘core’ regions, we observed region-specific two fiber families ranging between (−75°, −45°) and (45°, 75°) for the specimens of the proximal region, (−30°, −90°) and (30°, 90°) for the medial region, and (−60°, −90°) and (60°, 90°) for the distal region.

On the other hand, the fiber distribution for the proximal specimens (Fig. 8, *bottom panel* and Fig. S4) at the adventitia is not concentrated at a specific angle and partially covers the central region of the heat map, indicating a random distribution of fibers in this region. The medial region specimens showed a similar structure to the proximal ones, along with less pronounced overlap with the central region of the heat map and closer proximity to the ±90° boundary. Finally, the distal specimens showed very few fibers in the central region of the heat map and consistently showed high fiber frequency near the ±90° region, indicating a homogeneously aligned microstructure across the adventitia depth.

4. Discussion

4.1. Arterial Geometry

The left main coronary artery branches into the circumflex artery and the LADA. From the branching point onwards, we found that the diameter of the LADA decreases significantly from proximal to distal and that the wall thickness in the distal region is significantly smaller (Fig. 3(a)). In the literature, Bulant *et al.* [48] found that the human LADA radius decreases from 1.8 mm to 0.7 mm from proximal to distal, based on a computed coronary tomography

angiography. However, LADA wall thickness measurements are not consistently reported for specific regions. Gradus-Pizlo *et al.* [49] reported a wall thickness of 1.0 ± 0.2 mm for the medial region, which almost double our measurements. Perry *et al.* [50] found similar results using a method similar to Bulant *et al.,* suggesting that this error could be due to ultrasound techniques. On the other hand, *ex vivo* thickness measurements of the medial region were made by Holzapfel *et al.* [28], where a thickness of 0.83 ± 0.23 mm was found using a video extensometer. In general, our LADA geometrical measurements of the porcine LADA agree with the measurements in the literature for human specimens.

4.2. Region-Specific Biaxial Mechanical Properties

Overall, we observed the well-described anisotropic nonlinear stress-stretch response in all LADA regions [28, 45], where the tissue was consistently more extensive in the longitudinal direction than in the circumferential direction. Our findings included new observations in the *region-specific* mechanical behavior of the LADA and the decreasing circumferential extensibility from proximal to distal. We also observed that preconditioning of the LADA tissues resulted in a significantly greater stretch in the distal region, suggesting that this region may experience a larger pre-stretch *in vivo.* Arterial tissue undergoes pre-stretching to conserve energy over cardiac cycles [51, 52], and the degree of pre-stretching in the LADA has been reported to decrease with decreasing arterial diameter [53]. Because the pre-stretch is induced by elastic lamellae that are stretched during development [51, 54, 55], our pre-stretch results may be supported by the collagen-to-elastin ratio (i.e., lower in the distal region due to a thinner adventitia, Fig. S5). However, previous studies have not characterized the different regions of the epycardial part of the LADA, which limits the understanding of the pre-stretching behavior. Further research is needed to better extend this finding to the pre-stretch of the LADA.

The mechanical parameters obtained from the biaxial stress-stretch curves allowed a quantitative comparison of the behavior of the LADA regions. The E^{HT} values for all regions agreed with the values reported in the literature [56-58]. For example, Karimi *et al.* [58] found a maximum elastic modulus of 1.44 ± 0.87 MPa for human coronary arteries in uniaxial tests along the longitudinal direction, which agreed with our average E_L^{HT} of 1.16 ± 0.1 MPa (Table S1). On the other hand, human coronary artery values reported by Kural *et al.* [59] differed from our findings, likely due to age differences (44-81 years old) and comorbidity. Nonetheless, they found specimen-to-specimen variations in anisotropy, suggesting that reverse anisotropy (i.e., circumferential direction is more extensible than longitudinal) is a common feature in the tissues, as was also observed in our results (Fig. 3(c)). In our study, special attention was paid to the P_{CC}:P_{LL} = 1:0.5 loading ratio because of its well-known relation with the *in vivo* configuration [46, 47]. This loading ratio allowed us to further understand the anisotropic behavior of the LADA tissue. We observed that E^{LT} was homogeneous across the LADA regions; however, E^{HT} was significantly larger in the circumferential direction (Fig. 5). It is interesting to note that no significant differences in modulus measurements were observed between the LADA regions, although it was found that the median values for both E^{HT} and E^{LT} were lowest for the medial region. Furthermore, the constitutive model parameters showed similar trends (albeit different

numerical values) as the regional model described by Keyes *et al.* [38] where c increased in the proximal-to-distal direction and a_1 and a_2 increased in an opposite trend (Table S2).

Our experiments also yielded λ^* which represents the point at which crimped fibers become fully straight and are recruited as the main load-bearing components in the tissue [60]. This parameter showed a similar behavior as the moduli measurements over the loading ratios. We observed a median value for λ^* of about 1.2 that did not differ significantly between loading ratios. Interestingly, at the P_{CC}:P_{LL} = 1:0.5 loading ratio, λ^* was significantly greater at the longitudinal direction, indicating that the frequency of the crimped fibers is greater longitudinally than circumferentially oriented.

4.3. Characteristics of the Collagen Fiber Microstructure and the Load-Dependent Changes

Linking the microstructure to tissue biomechanics is fundamental to understand the mechanical requirements for CABG grafting and the design of TEVGs [45, 47]. In this study, we have characterized the load-dependent behavior of the collagen/elastin microstructure of the LADA. In contrast to previous studies, such as the study conducted by Chen *et al.* [61], we performed microstructural characterizations of the whole tissue at different loading points and under various loading ratios. First, we observed a consistent increase in DOA with increasing tissue stretch, indicating fiber uncrimping and fiber realignment towards a dominant loading direction [34]. The DOA increase was more pronounced in the proximal region but became less pronounced in the distal region and following a similar trend as the post-preconditioning stretch λ_c^*. The P_{CC}:P_{LL} = 1:0.5 loading ratio further clarifies this behavior, with the differences between the regions becoming more pronounced. These differences may be explained by: (i) the fiber orientation is more diverse (i.e., a more disperse distribution of θ_{fiber}) in the proximal region, allowing more reorientation toward a dominant loading direction; (ii) the fiber dispersion is reduced (i.e., more concentrated) in the post-preconditioning configuration for the medial and the distal regions, limiting fiber reorganization under load and ultimately DOA changes. These differences in fiber organization and load-dependent behavior may be caused by the different levels of blood pressure each region is exposed to *in vivo,* as shown by Fukunaga *et al.* [62]. They quantified a reduction of 15-20% in blood pressure from the ostium to the distal region. Furthermore, during the cardiac cycle, the distal region undergoes inward motion at higher in-plane velocities than the rest of the LADA [63], which may result in a reorganization of the adventitia microstructure as the artery approaches the apex.

The histograms of θ_{fiber} showed similar features (Fig. S2), where two common fiber families were observed. Our pSFDI-based results were similar to the multi-photon characterization performed by Chen *et al.* [61] where the adventitia was dissected from the remaining LADA layers and imaged under different biaxial loading conditions. In particular, they observed that fibers in the adventitia became highly aligned under longitudinally dominant loading. Our results using pSFDI and the bi-modal von Mises fit demonstrated similar behavior using whole-tissue biaxial loading for the different LADA regions. As can be seen in Fig. 7, the normalized angular distance between the two fiber families has been reduced under P_{CC}:P_{LL} = 0.25:1, which indicates that the fibers were longitudinally aligned. In contrast, a

circumferentially dominant loading (P_{CC}:P_{LL} = 1:0.25) would increase the distance between the two fiber families. For the distal region, we also observed a larger proportion of fibers with a small normalized angular distance (close to zero) in the PPC configuration, suggesting that the fibers for this region might be strongly aligned at their approximate *in vivo* configuration.

4.4. Unique Microstructural Features of the Distal LADA Region

Using multi-photon microscopy, we observed the common microstructure of the LADA (Fig. S3). We found that imaging of the vascular wall at the proximal region was consistent with previous studies [30, 64], but we also observed the region-specific features in the medial and distal regions. Overall, the proximal region showed the expected randomly distributed fiber architecture of the adventitia. Some proximal specimens showed a dominant fiber group oriented longitudinally (Fig. S3), although this was not a general trend. Furthermore, the medial region exhibited a fiber architecture that appeared to be a transition between the randomly distributed fiber arrangement of the proximal region to a clearly aligned architecture in the distal region, similar to the findings of Chen *et al.* [61]. To further compare the θ_{fiber} distribution of the entire vessel wall, we created heat maps that showing the location of the dominant fiber families at different tissue depths (Fig. 8 and Fig. S4). These results allowed to corroborate and confirm the observations on the unique microstructural load-dependent properties using pSFDI.

4.5. Study Limitations and Future Work

Soft tissue biomechanics is often limited by the great heterogeneity in the mechanical behavior of selected specimens, even when animal sources have controlled conditions. In this study, we aimed to characterize LADA tissues with a statistically meaningful sample size, for which we performed a preliminary analysis of the specimens and determined our final sample size based on these results. However, we still observed a large heterogeneity not only in terms of the measured mechanical parameters (see Section 3.2), but also in artery geometry (Fig. 3), heart size, and tortuosity (not measured) [65]. This lack of homogeneous measurements may lead to a lack of specificity when designing TEVGs. Another limitation of our biomechanical characterization lies in the *passive* conditions of our tests. Future studies using active stimulation of tunica media contraction will help to understand the active mechanical properties of the LADA regions. Finally, the coronary arteries are embedded in complex macrostructures that include connective tissue, fatty tissue, myocardium, and pericardium. All these structures play an important role in the passive and active properties of the LADA and need to be investigated.

Furthermore, misprediction in pSFDI-based microstructural characterization can be generated by tissue folding and the formation of bubbles during the imaging procedure: the latter is constantly monitored to reduce the possibility of this problem. Furthermore, the DOA is a metric directly related to the optical anisotropy of the imaged specimen, but not a direct physical metric like the normalized orientation index [37]. In this study, our pSFDI results were verified using multi-photon microscopy, which helped to overcome this limitation. Finally, the arterial tissues are not only passive biomechanically, but also actively

contract under sympathetic and parasympathetic responses [66, 67], which is an inherent limitation of our *ex vivo* biomechanical characterizations.

CABG surgery faces challenges in preventing graft failure when the graft does not match or resemble the geometry and mechanical properties of the target vessel [9-11]. Tissue engineering aims to address this urgent need, but TEVGs have not yet been translated for this application, mainly due to the mechanical mismatch with small-diameter target vessels. However, little attention has been paid to the specific microstructural features that anastomotic target sites may exhibit and require. The results of this study, such as the unique fiber organization at different regions of the vessel, the recruitment of fiber families under loading conditions and the biaxial mechanical parameters obtained here, elucidate the region-specific mechanical behavior and fiber architecture of the LADA and provide new insights into target parameters for the development of TEVGs. Our findings are supplemented by future research that investigates the longitudinal pre-stretch of the coronary arteries in a region-specific manner. These future characterizations will complement our current knowledge and also help advance current LADA constitutive models. Furthermore, the regional studies of other coronary arteries (e.g., left circumflex, right coronary artery) allow a more complete understanding of the vessel-specific properties for future systematic developments of patient-specific *in silico* modeling tools for CHD diagnostics and TEVG implantation.

4.6. Conclusion

The coronary arteries are fundamental vascular structures for cardiac physiology. In the present study, we have demonstrated that they are not only unique in terms of developmental and physiological perspective, but also have region-specific geometric, mechanical and microstructural features. Our experiments have led to the implications that LADA mechanics and microstructure vary along vessel length, shedding light on the new perspectives for clinical tool development for CABG. The characterized unique microstructural features of the LADA aid in the selection of autologous grafts as they should not only meet the geometric and mechanical parameters but also the tissue mechanics-microstructure linking of the native vessel. Furthermore, we expect that the current biomaterial synthesis techniques for VTE, such as electrospinning and decellularization, will find our results useful for future developments of TEVGs and anastomosis tools.

Supplementary Material

Refer to Web version on PubMed Central for supplementary material.

Acknowledgments.

We are deeply grateful for the support of Mr. Colton Ross for his invaluable contribution during study design. We would also like to acknowledge the American Heart Association Scientist Development Grant Award (16SDG27760143) and the Presbyterian Health Foundation Team Science Grant. S.A.P.-C. was supported in part by the Alumni Fellowship from the Graduate College at the University of Oklahoma. D.W.L. was supported by the National Science Foundation Graduate Research Fellowship (GRF 2019254233).

Appendix A.: Determination of θ_{fiber} and DOA from pSFDI Measurements

The gray-scale intensity (0-255) of polarization states was imported into an in-house MATLAB program to quantify the birefringent behavior pixel by pixel [34]. The intensity of each pixel was first fitted with a three-term Fourier series, i.e.

$$I = \alpha_0 + \alpha_2 [2 (\theta_{\text{fiber}} - \theta_{\text{polarizer}})] + \alpha_4 [4 (\theta_{\text{fiber}} - \theta_{\text{polarizer}})], \quad \text{(A.1)}$$

where α_0 denotes the mean light intensity, and α_2 and α_4 represent the polarization-dependent intensity changes. From this fit, the maximum intensity captures the polarization state in which the polarizer and the fiber angle match (i.e., $\theta_{\text{polarizer}} = \theta_{\text{fiber}}$). Next, the degree of local collagen fiber dispersion can be characterized by means of the degree of optical anisotropy (DOA), i.e.

$$\text{DOA} = \frac{\alpha_2 + \alpha_4}{\alpha_0 + \alpha_2 + \alpha_4}. \quad \text{(A.2)}$$

Figure A1 illustrates the load-dependent change in DOA (i.e. increase/decrease) for the three LADA regions under P_{CC}:P_{LL} = 1:1, P_{CC}:P_{LL} = 0.5:1, and P_{CC}:P_{LL} = 1:0.5 biaxial loading ratios.

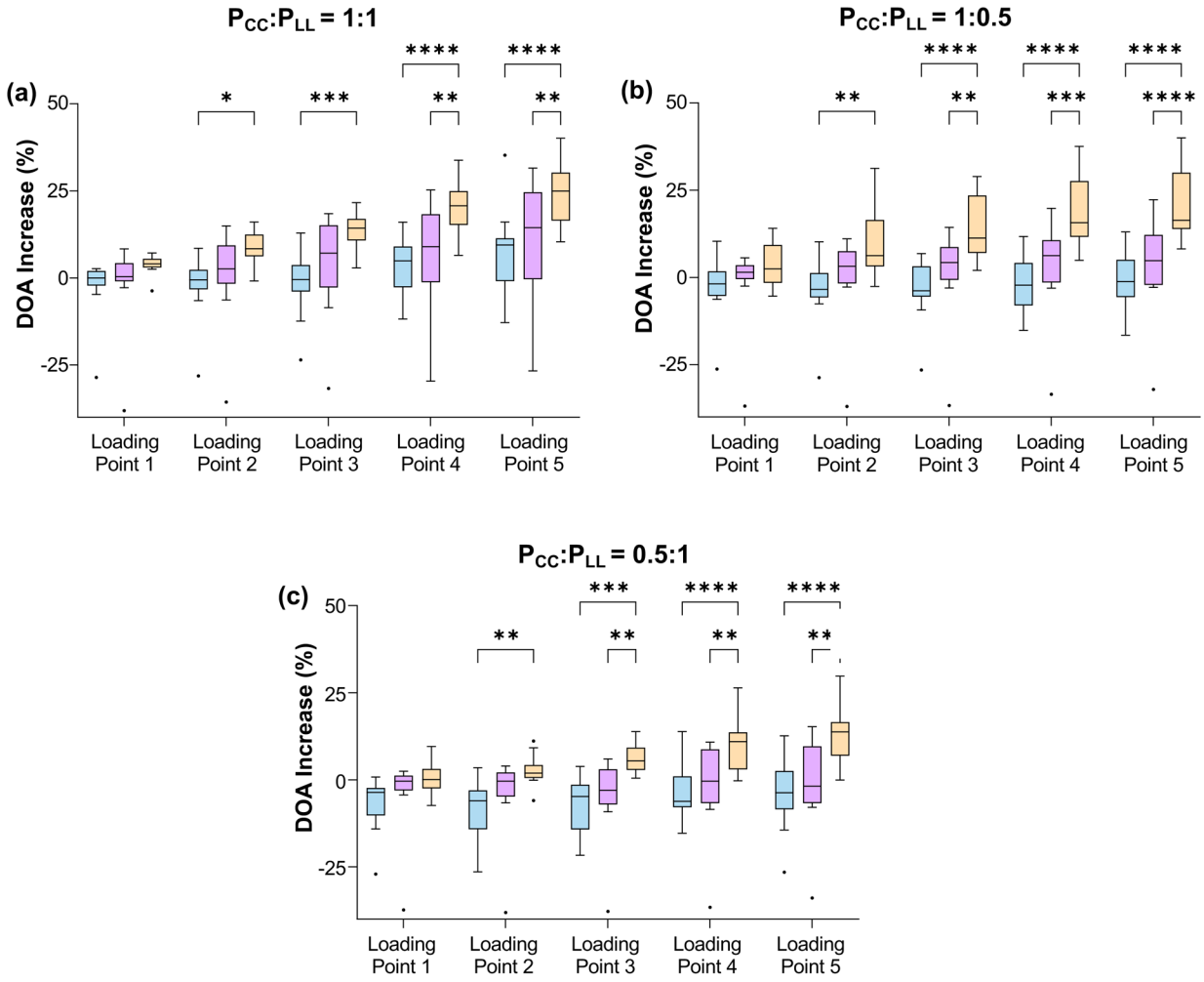

Figure A1: Load-dependent changes in the pSFDI-quantified degree of optical anisotropy (DOA) for the three LADA regions at different loading points under: (a) P_{CC}:P_{LL} = 1:1, (b) P_{CC}:P_{LL} = 1:0.5, and (c) P_{CC}:P_{LL} = 0.5:1. (Significance levels: * stands for $p < 0.05$, ** for $p < 0.01$, * * * for $p < 0.001$; black circles: data outliers; Circ. (C): circumferential, Long. (L): longitudinal directions)

Appendix B.: Bi-modal von Mises Fitting for Fiber Orientation Analysis

The quantification of θ_{fiber} led us to the postulation of two different fiber families in the LADA tissues (Section 3.3.1). For each fiber family, the orientation (μ_j's), dispersion (κ_j's), weight (w) and load-dependent changes can be further examined using a mixture bi-modal von Mises distribution, i.e.

$$f(\theta_{\text{fiber}} \mid \mu_1, \kappa_1, \mu_2, \kappa_2, w) = w g^{\text{V}-\text{M}}(\theta_{\text{fiber}} \mid \mu_1, \kappa_1) + (1-w) g^{\text{V}-\text{M}}(\theta_{\text{fiber}} \mid \mu_2, \kappa_2), \quad \text{(B.1)}$$

where $g^{\text{V}-\text{M}}(\theta \mid \mu, \kappa)$ is the π-periodic von Mises distribution with two parameters (μ, κ). Next, the normalized angular distance between fiber families, i.e., $| \mu_2 - \mu_1 | \ / \ 90^{\circ}$, and the weight ($w$) for the von Mises distribution mixture were determined for the PPC

configuration, peak equibiaxial loading (P_{CC}:P_{LL} = 1:1), and peak loading at other extreme loading ratios (P_{CC}:P_{LL} = 1:0.25 and P_{CC}:P_{LL} = 0.25:1), as demonstrated in Fig. 7.

References

[1]. Virani SS, Alonso A, Aparicio HJ, Benjamin EJ, Bittencourt MS, Callaway CW, Carson AP, Chamberlain AM, Cheng S, Delling FN, Elkind MS, Evenson KR, Ferguson JF, Gupta DK, Khan SS, Kissela BM, Knutson KL, Lee CD, Lewis TT, Liu J, Loop MS, Lutsey PL, Ma J, Mackey J, Martin SS, Matchar DB, Mussolino ME, Navaneethan SD, Perak AM, Roth GA, Samad Z, Satou GM, Schroeder EB, Shah SH, Shay CM, Stokes A, VanWagner LB, Wang N-Y, Tsao CW, On behalf of the American Heart Association Council on Epidemiology and Prevention Statistics Committee and Stroke Statistics Subcommittee, Heart Disease and Stroke Statistics-2021 Update, Circulation 143 (8) (2021) e254–e743. doi: 10.1161/CIR.0000000000000950. [PubMed: 33501848]

[2]. Jia S, Liu Y, Yuan J, Evidence in Guidelines for Treatment of Coronary Artery Disease, Springer Singapore, Singapore, 2020, Ch. 2, pp. 37–73. doi:10.1007/978-981-15-2517-9_2.

[3]. Khan MS, Coronary Artery Bypass Grafting: Surgical Anastomosis: Tips and Tricks, in: Murashita T (Ed.), The Current Perspectives on Coronary Artery Bypass Grafting, IntechOpen, Rijeka, 2020, Ch. 5, pp. 79–108. doi: 10.5772/intechopen.88932.

[4]. Fioranelli M, Roccia MG, Rovesti M, Satolli F, Petrelli P, Feliciani C, Lotti T, René Favaloro: The heart surgeon, Wiener Medizinische Wochenschrift 167 (1) (2017) 25–26. doi: 10.1007/s10354-017-0586-y.

[5]. Joo H-C, Youn Y-N, Yi G, Chang B-C, Yoo K-J, Off-pump bilateral internal thoracic artery grafting in right internal thoracic artery to right coronary system, The Annals of Thoracic Surgery 94 (3) (2012) 717–724. doi: 10.1016/j.athoracsur.2012.04.066. [PubMed: 22795885]

[6]. Tsuneyoshi H, Komiya T, Shimamoto T, Sakai J, Hiraoka T, Kawashima T, Muraoka G, Fujimoto M, Yamanaka K, The second best arterial graft to the left coronary system in off-pump bypass surgery: A propensity analysis of the radial artery with a proximal anastomosis to the ascending aorta versus the right internal thoracic artery, General Thoracic and Cardiovascular Surgery 63 (6) (2015) 335–342. doi: 10.1007/s11748-015-0534-y. [PubMed: 25836326]

[7]. Vuong NL, Elfaituri MK, Eldoadoa M, Karimzadeh S, Mokhtar MA, Eid PS, Nam NH, Mostafa MR, Radwan I, Zaki MMM, Al Khudari R, Kassem M, Huy NT, Saphenous vein harvesting techniques for coronary artery bypass grafting: a systematic review and meta-analysis, Coronary Artery Disease 33 (2) (2022). doi:10.1097/MCA.0000000000001048.

[8]. González Santos JM, López Rodríguez J, Dalmau Sorlí MJ, Arterial grafts in coronary surgery. treatment for everyone?, Revista Española de Cardiología 58 (10) (2005) 1207–23. doi:10.1016/S1885-5857(06)60400-3. [PubMed: 16238989]

[9]. Goldman S, Zadina K, Moritz T, Ovitt T, Sethi G, Copeland JG, Thottapurathu L, Krasnicka B, Ellis N, Anderson RJ, Henderson W, Long-term patency of saphenous vein and left internal mammary artery grafts after coronary artery bypass surgery: Results from a department of veterans affairs cooperative study, Journal of the American College of Cardiology 44 (11) (2004) 2149–2156. doi:10.1016/j.jacc.2004.08.064. [PubMed: 15582312]

[10]. Desai ND, Naylor CD, Kiss A, Cohen EA, Feder-Elituv R, Miwa S, Radhakrishnan S, Dubbin J, Schwartz L, Fremes SE, Impact of patient and target-vessel characteristics on arterial and venous bypass graft patency, Circulation 115 (6) (2007) 684–691. doi:10.1161/CIRCULATIONAHA.105.567495. [PubMed: 17283268]

[11]. Yamane Y, Uchida N, Okubo S, Morimoto H, Mukai S, Impact of the size mismatch between saphenous vein graft and coronary artery on graft patency, General Thoracic and Cardiovascular Surgery 65 (1) (2017) 25–31. doi: 10.1007/s11748-016-0694-4. [PubMed: 27485249]

[12]. Gaudino M, Antoniades C, Benedetto U, Deb S, Franco AD, Giammarco GD, Fremes S, Glineur D, Grau J, He G-W, Marinelli D, Ohmes LB, Patrono C, Puskas J, Tranbaugh R, Girardi LN, Taggart DP, Ruel M, Bakaeen FG, Mechanisms, consequences, and prevention of coronary graft failure, Circulation 136 (18) (2017) 1749–1764. doi:10.1161/CIRCULATIONAHA.117.027597. [PubMed: 29084780]

[13]. Hess CN, Lopes RD, Gibson CM, Hager R, Wojdyla DM, Englum BR, Mack MJ, Califf RM, Kouchoukos NT, Peterson ED, Alexander JH, Saphenous vein graft failure after coronary artery bypass surgery, Circulation 130 (17) (2014) 1445–1451. doi:10.1161/CIRCULATIONAHA.113.008193. [PubMed: 25261549]

[14]. Yaku H, Doi K, Redo coronary artery bypass grafting, General Thoracic and Cardiovascular Surgery 62 (8) (2014) 453–460. doi: 10.1007/s11748-014-0426-6. [PubMed: 24906816]

[15]. Lawson JH, Glickman MH, Ilzecki M, Jakimowicz T, Jaroszynski A, Peden EK, Pilgrim AJ, Prichard HL, Guziewicz M, Przywara S, Szmidt J, Turek J, Witkiewicz W, Zapotoczny N, Zubilewicz T, Niklason LE, Bioengineered human acellular vessels for dialysis access in patients with end-stage renal disease: two phase 2 single-arm trials, The Lancet 387 (10032) (2016) 2026–2034. doi:10.1016/S0140-6736(16)00557-2.

[16]. Dimitrievska S, Niklason LE, Historical perspective and future direction of blood vessel developments, Cold Spring Harbor Perspectives in Medicine 8 (2) (2018). doi:10.1101/cshperspect.a025742.

[17]. Fernández-Colino A, Wolf F, Rütten S, Schmitz-Rode T, Rodríguez-Cabello JC, Jockenhoevel S, Mela P, Small caliber compliant vascular grafts based on elastin-like recombinamers for in situ tissue engineering, Frontiers in Bioengineering and Biotechnology 7 (2019). doi:10.3389/fbioe.2019.00340.

[18]. Niklason LE, Lawson JH, Bioengineered human blood vessels, Science 370 (6513) (2020) eaaw8682. doi: 10.1126/science.aaw8682. [PubMed: 33033191]

[19]. Naito Y, Lee Y-U, Yi T, Church SN, Solomon D, Humphrey JD, Shin'oka T, Breuer CK, Beyond burst pressure: Initial evaluation of the natural history of the biaxial mechanical properties of tissue-engineered vascular grafts in the venous circulation using a murine model, Tissue Engineering Part A 20 (1-2) (2014) 346–355. doi: 10.1089/ten.tea.2012.0613. [PubMed: 23957852]

[20]. Pashneh-Tala S, MacNeil S, Claeyssens F, The tissue-engineered vascular graft—past, present, and future, Tissue Engineering Part B: Reviews 22 (1) (2016) 68–100. doi:10.1089/ten.teb.2015.0100. [PubMed: 26447530]

[21]. Saito J, Kaneko M, Ishikawa Y, Yokoyama U, Challenges and possibilities of cell-based tissue-engineered vascular grafts, Cyborg and Bionic Systems 2021 (2021) 1532103. doi:10.34133/2021/1532103. [PubMed: 36285145]

[22]. Ravulapalli HB, Karthekeyan RB, Vakumudi M, Srigiri R, Saldanha R, Sulaiman S, Intraoperative anastomotic site detection and assessment of LIMA-to-LAD anastomosis by epicardial ultrasound in off-pump coronary artery bypass grafting-A prospective single-blinded study, Annals of Cardiac Anaesthesia 13 (3) (2010) 231–5. doi: 10.4103/0971-9784.69069. [PubMed: 20826964]

[23]. Li H, Xie B, Gu C, Gao M, Zhang F, Wang J, Dai L, Yu Y, Distal end side-to-side anastomoses of sequential vein graft to small target coronary arteries improve intraoperative graft flow, BMC Cardiovascular Disorders 14 (1) (2014) 65. doi:10.1186/1471-2261-14-65. [PubMed: 24884776]

[24]. Papamanolis L, Kim HJ, Jaquet C, Sinclair M, Schaap M, Danad I, van Diemen P, Knaapen P, Najman L, Talbot H, Taylor CA, Vignon-Clementel I, Myocardial perfusion simulation for coronary artery disease: A coupled patient-specific multiscale model, Annals of Biomedical Engineering 49 (5) (2021) 1432–1447. doi:10.1007/s10439-020-02681-z. [PubMed: 33263155]

[25]. Blum KM, Zbinden JC, Ramachandra AB, Lindsey SE, Szafron JM, Reinhardt JW, Heitkemper M, Best CA, Mirhaidari GJM, Chang Y-C, Ulziibayar A, Kelly J, Shah KV, Drews JD, Zakko J, Miyamoto S, Matsuzaki Y, Iwaki R, Ahmad H, Daulton R, Musgrave D, Wiet MG, Heuer E, Lawson E, Schwarz E, McDermott MR, Krishnamurthy R, Krishnamurthy R, Hor K, Armstrong AK, Boe BA, Berman DP, Trask AJ, Humphrey JD, Marsden AL, Shinoka T, Breuer CK, Tissue engineered vascular grafts transform into autologous neovessels capable of native function and growth, Communications Medicine 2 (1) (2022) 3. doi: 10.1038/s43856-021-00063-7. [PubMed: 35603301]

[26]. Drews JD, Pepper VK, Best CA, Szafron JM, Cheatham JP, Yates AR, Hor KN, Zbinden JC, Chang Y-C, Mirhaidari GJM, Ramachandra AB, Miyamoto S, Blum KM, Onwuka EA, Zakko J, Kelly J, Cheatham SL, King N, Reinhardt JW, Sugiura T, Miyachi H, Matsuzaki Y, Breuer J, Heuer ED, West TA, Shoji T, Berman D, Boe BA, Asnes J, Galantowicz M, Matsumura G,

Hibino N, Marsden AL, Pober JS, Humphrey JD, Shinoka T, Breuer CK, Spontaneous reversal of stenosis in tissue-engineered vascular grafts, Science translational medicine 12 (537) (2020) eaax6919. doi:10.1126/scitranslmed.aax6919. [PubMed: 32238576]

[27]. Duginski GA, Ross CJ, Laurence DW, Johns CH, Lee C-H, An investigation of the effect of freezing storage on the biaxial mechanical properties of excised porcine tricuspid valve anterior leaflets, Journal of the Mechanical Behavior of Biomedical Materials 101 (2020) 103438. doi:10.1016/j.jmbbm.2019.103438. [PubMed: 31542570]

[28]. Holzapfel GA, Sommer G, Gasser CT, Regitnig P, Determination of layer-specific mechanical properties of human coronary arteries with nonatherosclerotic intimal thickening and related constitutive modeling, American Journal of Physiology-Heart and Circulatory Physiology 289 (5) (2005) H2048–H2058. doi:10.1152/ajpheart.00934.2004. [PubMed: 16006541]

[29]. Cheng S, Clarke EC, Bilston LE, The effects of preconditioning strain on measured tissue properties, Journal of Biomechanics 42 (9) (2009) 1360–1362. doi:10.1016/j.jbiomech.2009.03.023. [PubMed: 19394022]

[30]. Chen H, Liu Y, Slipchenko M, Zhao X, Cheng J-X, Kassab G, The layered structure of coronary adventitia under mechanical load, Biophysical Journal 101 (11) (2011) 2555–2562. doi:10.1016/j.bpj.2011.10.043. [PubMed: 22261042]

[31]. Jett S, Laurence D, Kunkel R, Babu AR, Kramer K, Baumwart R, Towner R, Wu Y, Lee C-H, An investigation of the anisotropic mechanical properties and anatomical structure of porcine atrioventricular heart valves, Journal of the Mechanical Behavior of Biomedical Materials 87 (2018) 155–171. doi:10.1016/j.jmbbm.2018.07.024. [PubMed: 30071486]

[32]. Ross CJ, Laurence DW, Echols AL, Babu AR, Gu T, Duginski GA, Johns CH, Mullins BT, Casey KM, Laurence KA, Zhao YD, Amini R, Fung K-M, Mir A, Burkhart HM, Wu Y, Holzapfel GA, Lee C-H, Effects of enzyme-based removal of collagen and elastin constituents on the biaxial mechanical responses of porcine atrioventricular heart valve anterior leaflets, Acta Biomaterialia 135 (2021) 425–440. doi:10.1016/j.actbio.2021.08.043. [PubMed: 34481053]

[33]. Labrosse MR, Jafar R, Ngu J, Boodhwani M, Planar biaxial testing of heart valve cusp replacement biomaterials: Experiments, theory and material constants, Acta Biomaterialia 45 (2016) 303–320. doi:10.1016/j.actbio.2016.08.036. [PubMed: 27570204]

[34]. Jett SV, Hudson LT, Baumwart R, Bohnstedt BN, Mir A, Burkhart HM, Holzapfel GA, Wu Y, Lee C-H, Integration of polarized spatial frequency domain imaging (pSFDI) with a biaxial mechanical testing system for quantification of load-dependent collagen architecture in soft collagenous tissues, Acta Biomaterialia 102 (2020) 149–168. doi:10.1016/j.actbio.2019.11.028. [PubMed: 31734412]

[35]. Laurence DW, Homburg H, Yan F, Tang Q, Fung K-M, Bohnstedt BN, Holzapfel GA, Lee C-H, A pilot study on biaxial mechanical, collagen microstructural, and morphological characterizations of a resected human intracranial aneurysm tissue, Scientific reports 11 (1) (2021) 1–15. [PubMed: 33414495]

[36]. Yang B, Lesicko J, Sharma M, Hill M, Sacks MS, Tunnell JW, Polarized light spatial frequency domain imaging for non-destructive quantification of soft tissue fibrous structures, Biomedical Optics Express 6 (4) (2015) 1520–1533. doi:10.1364/BOE.6.001520. [PubMed: 25909033]

[37]. Goth W, Potter S, Allen ACB, Zoldan J, Sacks MS, Tunnell JW, Non-destructive reflectance mapping of collagen fiber alignment in heart valve leaflets, Annals of Biomedical Engineering 47 (5) (2019) 1250–1264. doi:10.1007/s10439-019-02233-0. [PubMed: 30783832]

[38]. Keyes JT, Lockwood DR, Simon BR, Van de Geest JP, Deformationally dependent fluid transport properties of porcine coronary arteries based on location in the coronary vasculature, Journal of the Mechanical Behavior of Biomedical Materials 17 (2013) 296–306. doi:10.1016/j.jmbbm.2012.10.002. [PubMed: 23127633]

[39]. Yu W-J, Shen M, Chen W-N, Zhan Z-H, Gong Y-J, Lin Y, Liu O, Zhang J, Differential evolution with two-level parameter adaptation, IEEE Transactions on Cybernetics 44 (7) (2014) 1080–1099. doi:10.1109/TCYB.2013.2279211. [PubMed: 24013834]

[40]. Calle EA, Vesuna S, Dimitrievska S, Zhou K, Huang A, Zhao L, Niklason LE, Levene MJ, The use of optical clearing and multiphoton microscopy for investigation of three-dimensional tissue-engineered constructs, Tissue Engineering Part C: Methods 20 (7) (2014) 570–577. doi:10.1089/ten.tec.2013.0538. [PubMed: 24251630]

[41]. Rezakhaniha R, Agianniotis A, Schrauwen J, Griffa A, Sage D, Bouten C, van de Vosse F, Unser M, Stergiopulos N, Experimental investigation of collagen waviness and orientation in the arterial adventitia using confocal laser scanning microscopy, Biomechanics and Modeling in Mechanobiology 11 (3-4) (2012) 461–473. doi:10.1007/s10237-011-0325-z. [PubMed: 21744269]

[42]. Schindelin J, Arganda-Carreras I, Frise E, Kaynig V, Longair M, Pietzsch T, Preibisch S, Rueden C, Saalfeld S, Schmid B, Tinevez J-Y, White DJ, Hartenstein V, Eliceiri K, Tomancak P, Cardona A, Fiji: an open-source platform for biological-image analysis, Nature Methods 9 (7) (2012) 676–682. doi:10.1038/nmeth.2019. [PubMed: 22743772]

[43]. Erdfelder E, Faul F, Buchner A, Gpower: A general power analysis program, Behavior Research Methods, Instruments & Computers 28 (1) (1996) 1–11. doi:10.3758/BF03203630.

[44]. Wobbrock JO, Findlater L, Gergle D, Higgins JJ, The aligned rank transform for nonparametric factorial analyses using only anova procedures, in: Proceedings of the SIGCHI Conference on Human Factors in Computing Systems, Association for Computing Machinery, New York, NY, USA, 2011, p. 143–146. doi:10.1145/1978942.1978963.

[45]. Chen H, Kassab GS, Microstructure-based biomechanics of coronary arteries in health and disease, Journal of Biomechanics 49 (12) (2016) 2548–2559. doi:10.1016/j.jbiomech.2016.03.023. [PubMed: 27086118]

[46]. Huo Y, Cheng Y, Zhao X, Lu X, Kassab GS, Biaxial vasoactivity of porcine coronary artery, American Journal of Physiology-Heart and Circulatory Physiology 302 (10) (2012) H2058–H2063. doi:10.1152/ajpheart.00758.2011. [PubMed: 22427520]

[47]. Camasão D, Mantovani D, The mechanical characterization of blood vessels and their substitutes in the continuous quest for physiological-relevant performances. A critical review, Materials Today Bio 10 (2021) 100106. doi: 10.1016/j.mtbio.2021.100106.

[48]. Bulant C, Blanco P, Clausse A, Assunção A, Lima T, Ávila L, Feijóo R, Lemos P, Association between three-dimensional vessel geometry and the presence of atherosclerotic plaques in the left anterior descending coronary artery of high-risk patients, Biomedical Signal Processing and Control 31 (2017) 569–575. doi:10.1016/j.bspc.2016.09.023.

[49]. Gradus-Pizlo I, Bigelow B, Mahomed Y, Sawada SG, Rieger K, Feigenbaum H, Left anterior descending coronary artery wall thickness measured by high-frequency transthoracic and epicardial echocardiography includes adventitia, American Journal of Cardiology 91 (1) (2003) 27–32. doi:10.1016/s0002-9149(02)02993-4. [PubMed: 12505567]

[50]. Perry R, Joseph MX, Chew DP, Aylward PE, De Pasquale CG, Coronary artery wall thickness of the left anterior descending artery using high resolution transthoracic echocardiography – Normal range of values, Echocardiography 30 (7) (2013) 759–764. doi:10.1111/echo.12136. [PubMed: 23346915]

[51]. Humphrey J, Eberth J, Dye W, Gleason R, Fundamental role of axial stress in compensatory adaptations by arteries, Journal of Biomechanics 42 (1) (2009) 1–8. doi:10.1016/j.jbiomech.2008.11.011. [PubMed: 19070860]

[52]. Kamenskiy AV, Pipinos II, Dzenis YA, Phillips NY, Desyatova AS, Kitson J, Bowen R, Mac-Taggart JN, Effects of age on the physiological and mechanical characteristics of human femoropopliteal arteries, Acta Biomaterialia 11 (2015) 304–313. doi:10.1016/j.actbio.2014.09.050. [PubMed: 25301303]

[53]. Guo X, Liu Y, Kassab GS, Diameter-dependent axial prestretch of porcine coronary arteries and veins, Journal of Applied Physiology 112 (6) (2012) 982–989. doi:10.1152/japplphysiol.00857.2011. [PubMed: 22162531]

[54]. Davis EC, Elastic lamina growth in the developing mouse aorta., Journal of Histochemistry & Cytochemistry 43 (11) (1995) 1115–1123. doi:10.1177/43.11.7560894. [PubMed: 7560894]

[55]. Cardamone L, Valentín A, Eberth JF, Humphrey JD, Origin of axial prestretch and residual stress in arteries, Biomechanics and Modeling in Mechanobiology 8 (6) (2009) 431. doi: 10.1007/s10237-008-0146-x. [PubMed: 19123012]

[56]. Lu X, Pandit A, Kassab GS, Biaxial incremental homeostatic elastic moduli of coronary artery: Two-layer model, American Journal of Physiology-Heart and Circulatory Physiology 287 (4) (2004) H1663–H1669. doi:10.1152/ajpheart.00226.2004. [PubMed: 15371266]

[57]. Chen H, Luo T, Zhao X, Lu X, Huo Y, Kassab GS, Microstructural constitutive model of active coronary media, Biomaterials 34 (31) (2013) 7575–7583. doi:10.1016/j.biomaterials.2013.06.035. [PubMed: 23859656]

[58]. Karimi A, Navidbakhsh M, Shojaei A, Faghihi S, Measurement of the uniaxial mechanical properties of healthy and atherosclerotic human coronary arteries, Materials Science and Engineering: C 33 (5) (2013) 2550–2554. doi: 10.1016/j.msec.2013.02.016. [PubMed: 23623067]

[59]. Kural MH, Cai M, Tang D, Gwyther T, Zheng J, Billiar KL, Planar biaxial characterization of diseased human coronary and carotid arteries for computational modeling, Journal of Biomechanics 45 (5) (2012) 790–798. doi: 10.1016/j.jbiomech.2011.11.019. [PubMed: 22236530]

[60]. Hill MR, Duan X, Gibson GA, Watkins S, Robertson AM, A theoretical and non-destructive experimental approach for direct inclusion of measured collagen orientation and recruitment into mechanical models of the artery wall, Journal of Biomechanics 45 (5) (2012) 762–771. doi:10.1016/j.jbiomech.2011.11.016. [PubMed: 22305290]

[61]. Chen H, Slipchenko MN, Liu Y, Zhao X, Cheng J-X, Lanir Y, Kassab GS, Biaxial deformation of collagen and elastin fibers in coronary adventitia, Journal of Applied Physiology 115 (11) (2013) 1683–1693. doi:10.1152/japplphysiol.00601.2013. [PubMed: 24092692]

[62]. Fukunaga M, Fujii K, Mintz GS, Kawasaki D, Nakata T, Miki K, Imanaka T, Tamaru H, Shibuya M, Masuyama T, Distribution of pressure gradients along the left anterior descending artery in patients with angiographically normal arteries, Catheterization and Cardiovascular Interventions 96 (1) (2020) E67–E74. doi: 10.1002/ccd.28544. [PubMed: 31609096]

[63]. Shechter G, Resar J, McVeigh E, Displacement and velocity of the coronary arteries: Cardiac and respiratory motion, IEEE Transactions on Medical Imaging 25 (3) (2006) 369–375. doi:10.1109/TMI.2005.862752. [PubMed: 16524092]

[64]. Zoumi A, Lu X, Kassab GS, Tromberg BJ, Imaging coronary artery microstructure using second-harmonic and two-photon fluorescence microscopy, Biophysical Journal 87 (4) (2004) 2778–2786. doi:10.1529/biophysj.104.042887. [PubMed: 15454469]

[65]. Zhu H, Ding Z, Piana RN, Gehrig TR, Friedman MH, Cataloguing the geometry of the human coronary arteries: A potential tool for predicting risk of coronary artery disease, International Journal of Cardiology 135 (1) (2009)43–52. doi:10.1016/j.ijcard.2008.03.087. [PubMed: 18597872]

[66]. Lu Y, Wu H, Li J, Gong Y, Ma J, Kassab GS, Huo Y, Tan W, Huo Y, Passive and active triaxial wall mechanics in a two-layer model of porcine coronary artery, Scientific Reports 7 (1) (2017) 13911. doi: 10.1038/s41598-017-14276-1. [PubMed: 29066847]

[67]. Halper J, Basic components of vascular connective tissue and extracellular matrix, Advances in Pharmacology 81 (2018) 95–127. doi:10.1016/bs.apha.2017.08.012 [PubMed: 29310805]

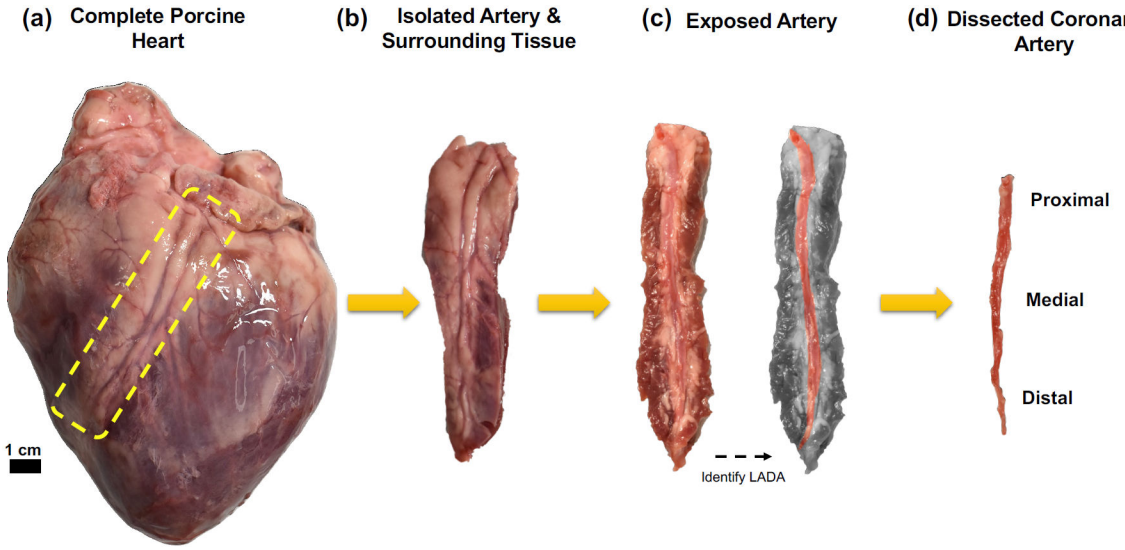

Figure 1:

Photographs showing the procedure for dissecting the left anterior descending artery (LADA) tissues: (a) the whole porcine heart (the dashed line indicates the area where the incisions were made to expose the artery and its surrounding tissue), (b) the isolated myocardium and adipose tissues surrounding the coronary artery, (c) a visual representation of how the artery was identified to further dissect the surrounding tissue, and (d) the dissected LADA and three regions for biaxial mechanical and microstructural characterizations.

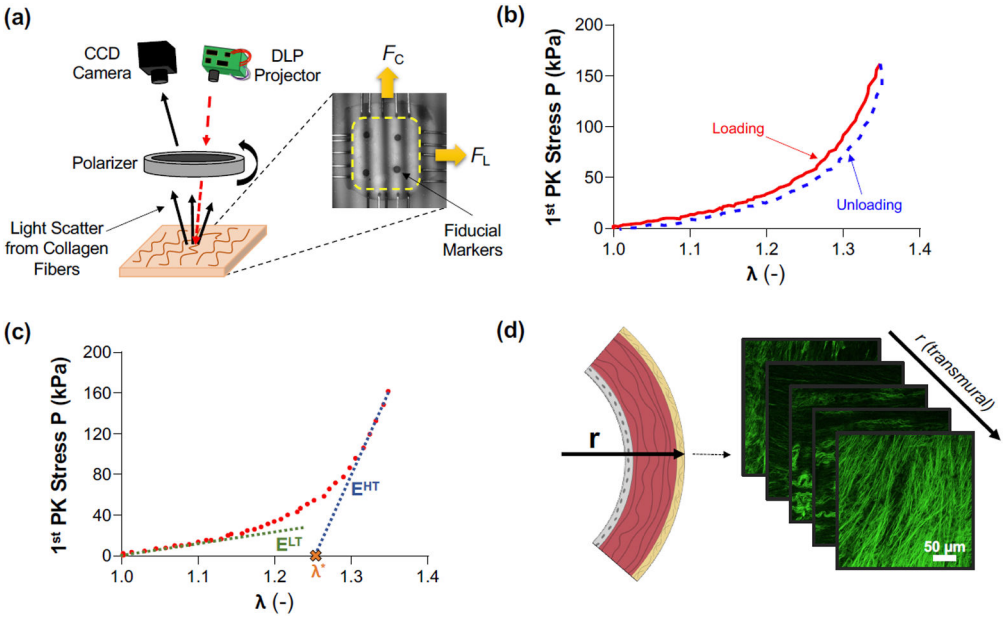

Figure 2:

Schematic of the characterizations of the region-specific LADA specimens: (a) LADA specimen mounted on a biaxial testing system using BioRakes (*photo*) showing an effective test region (*yellow dashed line*), that was integrated with an in-house collagen microstructural quantification device; (b) representative loading-unloading curve for the LADA tissues, showing the characteristic narrow hysteresis; (c) determination of the low- and high-tension elastic moduli (E^{LT}, E^{HT}) and tissue extensibility (λ^*); (d) illustration of the arterial wall, the three investigated layers, and the defined radial direction (*left*) and representative multi-photon microscopy images at different tissue depths (*right*).

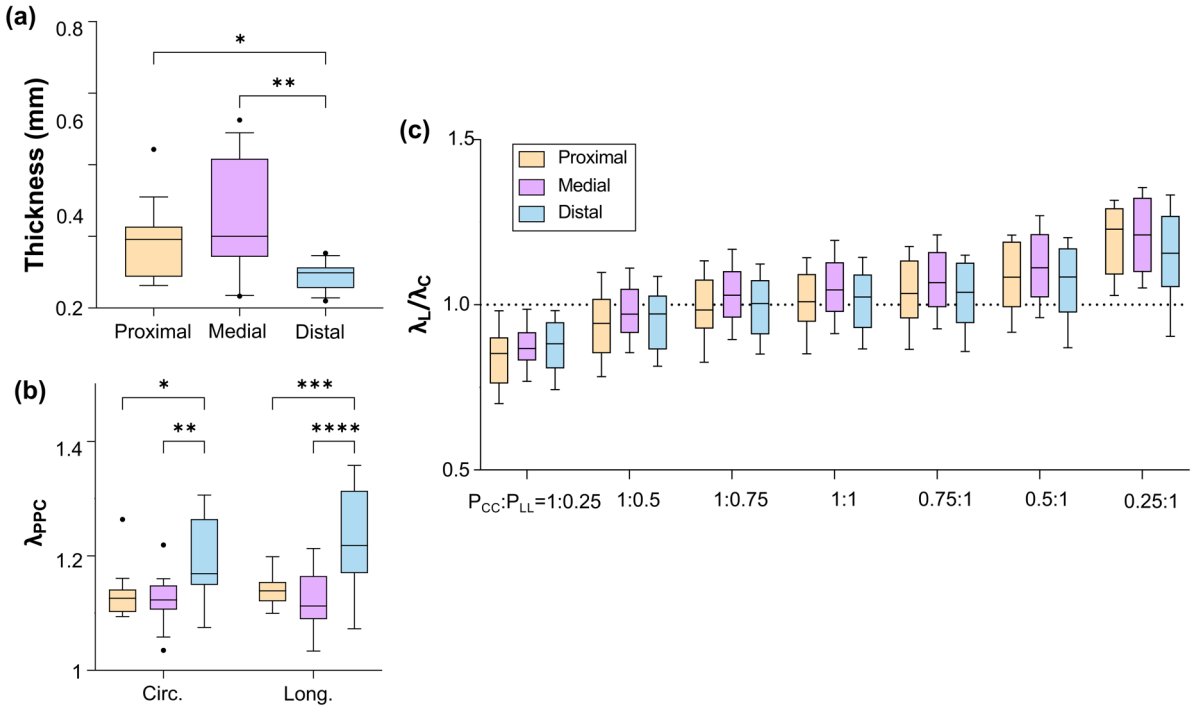

Figure 3:

(a) Thickness measurements, (b) stretch after preconditioning (λ_{PPC}), and (c) ratios between the longitudinal (λ_L) and circumferential (λ_C) stretches at various biaxial stress ratios (P_{CC}: P_{LL}) for the three LADA regions. (Significance levels: * for $p < 0.05$, ** for $p < 0.01$, * * * for $p < 0.001$; black circles: data outliers; Circ. (C): circumferential, Long. (L): longitudinal directions)

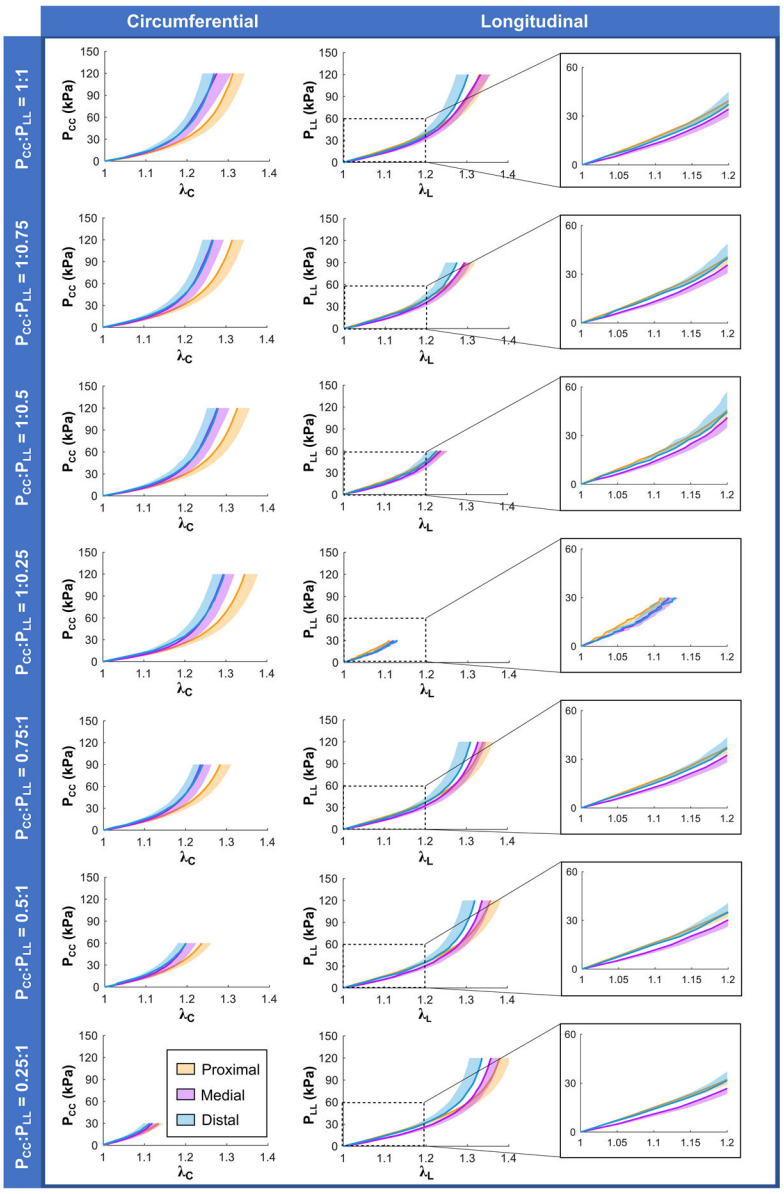

Figure 4:

Stress-stretch results for the LADA regions in the circumferential (*left column*) and longitudinal (*right column*) directions under various biaxial loading ratios (solid curves: the mean, shaded areas: half of the standard error of the mean – SEM).

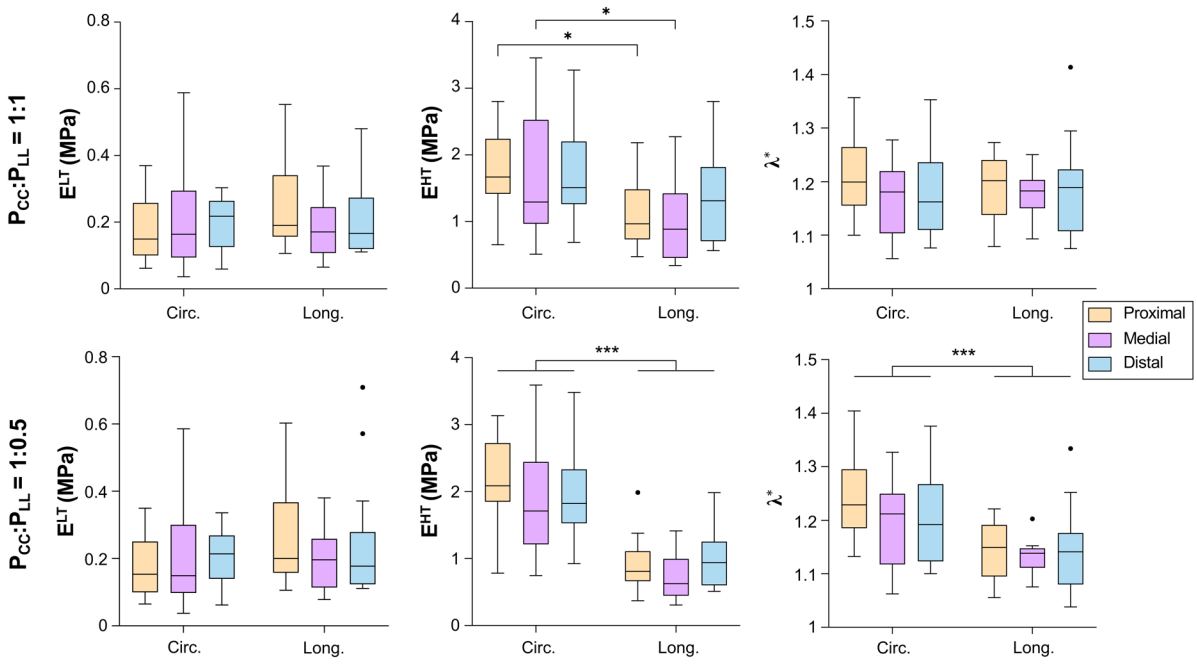

Figure 5:

Mechanical parameters from the individual stress-stretch curves for the $P_{CC}:P_{LL} = 1:1$ (*top row*) and $P_{CC}:P_{LL} = 1:0.5$ (*bottom row*) loading ratios: low-tension and high-tension modulus and tissue extensibility. (Significance levels: * for $p < 0.05$, * * * for $p < 0.001$; black circles: data outliers; Circ. (C): circumferential, Long. (L): longitudinal directions)

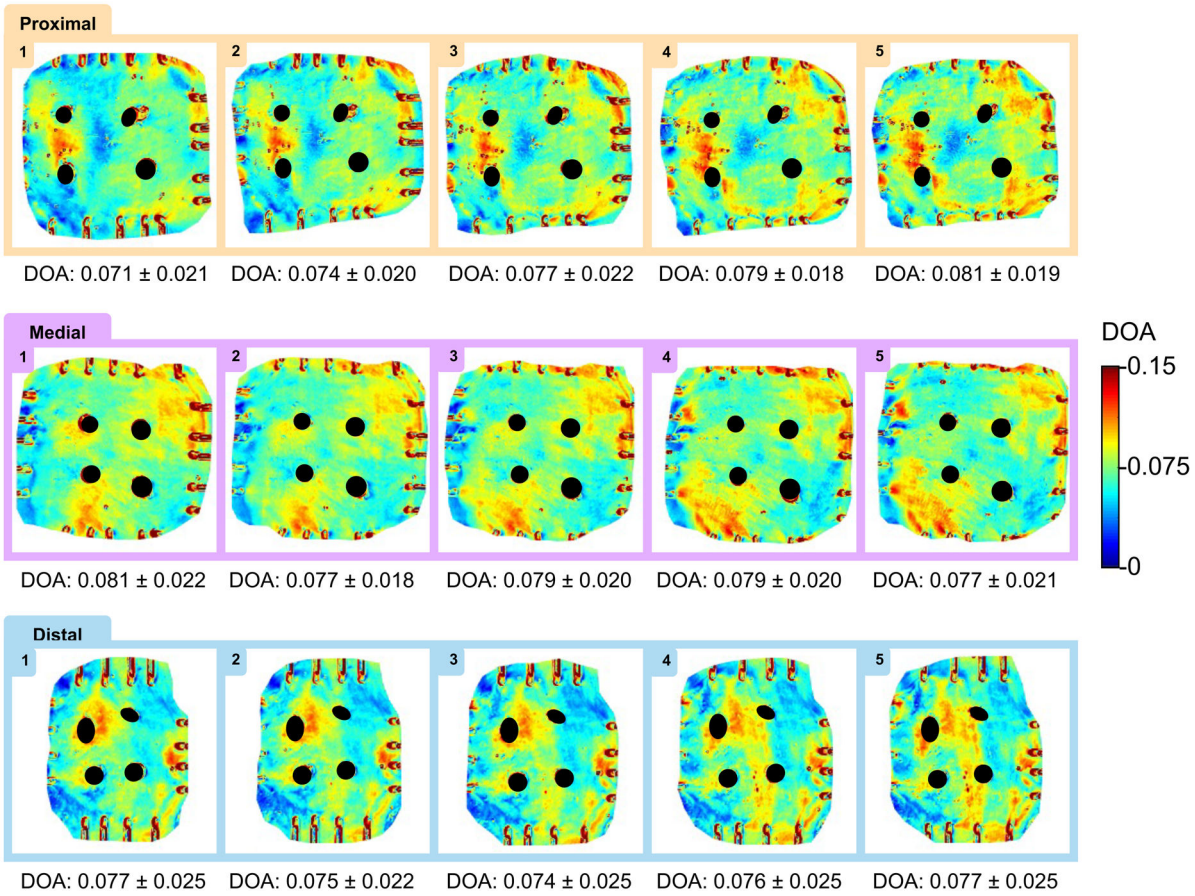

Figure 6:

Representative degree of optical anisotropy (DOA) maps of the three LADA tissue regions at different loading points under equibiaxial tension (P_{CC}: P_{LL} = 1:1).

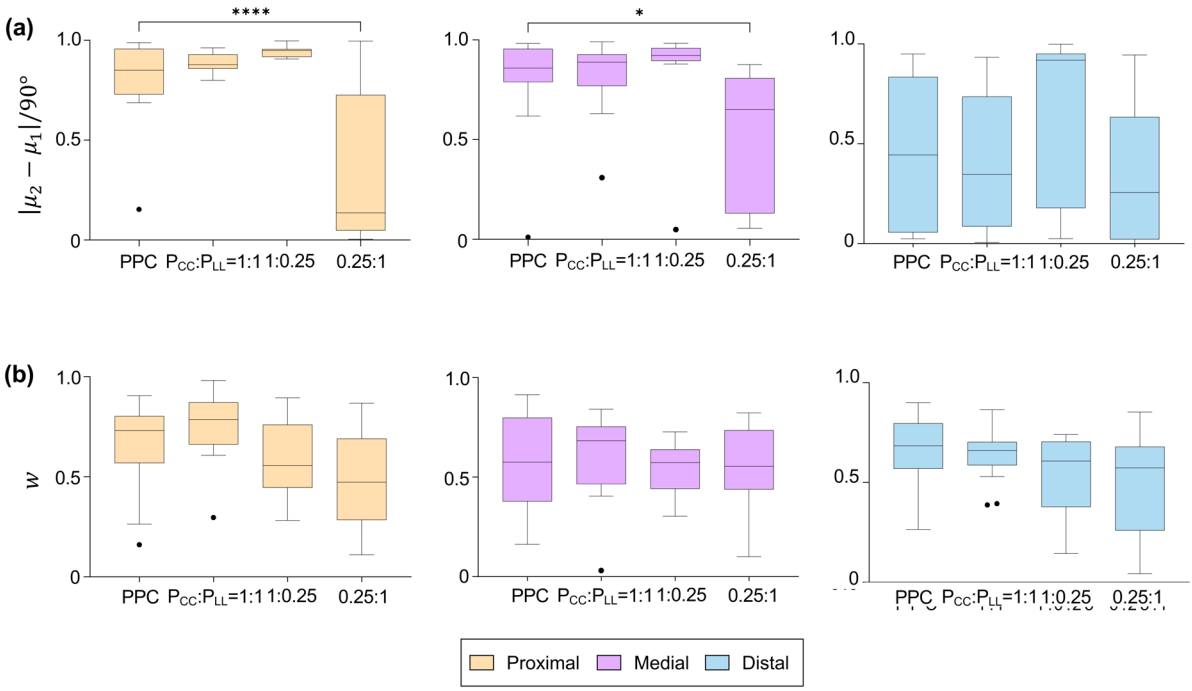

Figure 7:

Parameters of the bi-modal von Mises fit for the pSFDI-quantified θ_{fiber} at post-preconditioning (PPC), equibiaxial tension and extreme loading ratios: (a) the normalized angular distance of the fiber orientation; (b) the weight for the first fiber family. (Significance levels: * for $p < 0.05$, * * * for $p < 0.001$; black circles: data outliers; Circ. (C): circumferential, Long. (L): longitudinal directions)

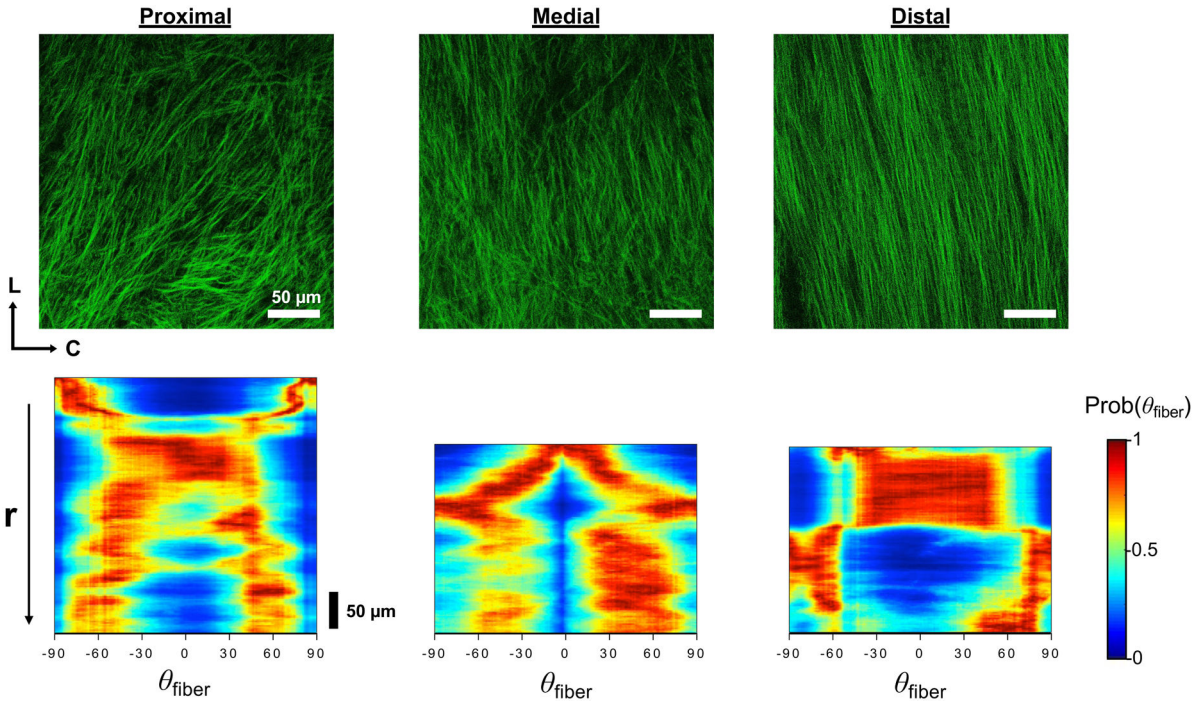

Figure 8:

(*top row*) Multi-photon micrographs of the tunica adventitia of the LADA regions (*bottom row*). Heat map representation of normalized fiber frequency across the depth of the vessel.